Analysis of the Regional Ionosphere at Low Latitudes in Support of the Biomass ESA Mission

Lucilla Alfonsi, Gabriella Povero, Luca Spogli, Claudio Cesaroni, Biagio Forte, Cathryn N. Mitchell, Robert Burston, Sreeja Vadakke Veettil, Marcio Aquino, Virginia Klausner, Marcio T. A. H. Muella, Michael Pezzopane, Alessandra Giuntini, Ingrid Hunstad, Giorgiana De Franceschi, Elvira Musicò, Marco Pini, Vinh La The, Hieu Tran Trung, Asnawi Husin, Sri Ekawati, Charisma Victoria de la Cruz-Cayapan, Mardina Abdullah, Noridawaty Mat Daud, Le Huy Minh, and Nicolas Floury

***Abstract*— Biomass is a spaceborn polarimetric P-band (435 MHz) synthetic aperture radar (SAR) in a dawn–dusk low Earth orbit. Its principal objective is to measure biomass content and change in all the Earth's forests. The ionosphere introduces the Faraday rotation on every pulse emitted by low-frequency SAR and scintillations when the pulse traverses a region of plasma irregularities, consequently impacting the quality of the imaging. Some of these effects are due to total electron content (TEC) and its gradients along the propagation path. Therefore, an accurate assessment of the ionospheric morphology and dynamics is necessary to properly understand the impact on image quality, especially in the equatorial and tropical regions. To this scope, we have conducted an in-depth investigation of the significant noise budget introduced by the two crests of the equatorial ionospheric anomaly (EIA) over Brazil and Southeast Asia. This paper is characterized by a novel approach to conceive a SAR-oriented ionospheric assessment, aimed at detecting and identifying spatial and temporal TEC gradients, including scintillation effects and traveling ionospheric disturbances, by means of Global Navigation Satellite Systems ground-based monitoring stations. The novelty of this approach resides in the customization of the information about the impact of the ionosphere on SAR imaging as derived by local dense networks of ground instruments operating during the passes of Biomass spacecraft. The results identify the EIA crests as the regions hosting the bulk of irregularities potentially causing degradation on SAR imaging. Interesting insights about the local characteristics of low-latitudes ionosphere are also highlighted.**

***Index Terms*— Equatorial ionospheric anomaly (EIA), ionospheric climatology, ionospheric impact on synthetic aperture radar (SAR), total electron content (TEC) gradients.**

Manuscript received December 27, 2017; revised February 20, 2018; accepted April 22, 2018. Date of publication June 21, 2018; date of current version October 25, 2018. This work was supported by the European Space Agency through the Alcantara Initiative of the General Study Program through two projects: Ionospheric Research for Biomass in South America (ESA) under Contract 4000117287/16/F/MOS and Ionospheric Environment Characterization for Biomass Calibration Over South East Asia (ESA) under Contract 4000117285/16/F/MOS. The work of C. Mitchell was supported by the U.K. NERC under Grant NE/P006450/1. *(Corresponding author: Lucilla Alfonsi.)*

L. Alfonsi, C. Cesaroni, M. Pezzopane, A. Giuntini, I. Hunstad, and G. De Franceschi are with the Istituto Nazionale di Geofisica e Vulcanologia, 00143 Rome, Italy (e-mail: lucilla.alfonsi@ingv.it; claudio.cesaroni@ingv.it; michael.pezzopane@ingv.it; alessandra.giuntini@ingv.it; ingrid.hunstad@ingv.it; giorgiana.defranceschi@ingv.it; elvira.musico@ingv.it).

G. Povero and M. Pini are with the Istituto Superiore Mario Boella, 10138 Turin, Italy (e-mail: gabriella.povero@ismb.it; marco.pini@ismb.it).

L. Spogli is with the Istituto Nazionale di Geofisica e Vulcanologia, 00143 Rome, Italy, and also with SpacEarth Technology, 00143 Rome, Italy (e-mail: luca.spogli@ingv.it).

B. Forte, C. N. Mitchell, and R. Burston are with the University of Bath, Bath BA2 7AN, U.K. (e-mail: b.forte@bath.ac.uk; rjb22@bath.ac.uk; c.n.mitchell@bath.ac.uk).

S. V. Veettil and M. Aquino are with the University of Nottingham, Nottingham NG7 2TU, U.K. (e-mail: sreejavadakke.veettil@nottingham.ac.uk; marcio.aquino@nottingham.ac.uk).

V. Klausner and M. T. A. H. Muella are with the Instituto de Pesquisa e Desenvolvimento, Universidade do Vale do Paraíba, São José dos Campos 12244-000, Brazil (e-mail: virginia@univap.br; mmuella@univap.br).

E. Musicò is with the Istituto Nazionale di Geofisica e Vulcanologia, 00143 Rome, Italy, and also with the Sapienza University of Rome, 00185 Rome, Italy.

V. La The and H. Tran Trung are with the Hanoi University of Science and Technology, Hanoi 112408, Vietnam (e-mail: vinh.lathe@hust.edu.vn; hieu.trantrung-navis@hust.edu.vn).

A. Husin and S. Ekawati are with the National Institute of Aeronautics and Space, Jakarta 40173, Indonesia (e-mail: asnawi@lapan.go.id; sri.ekawati@lapan.go.id).

C. V. de la Cruz-Cayapan is with the National Mapping and Resource Information Authority, Taguig 1634, Philippines (e-mail: cvdcayapan@namria.gov.ph).

M. Abdullah and N. Mat Daud are with the Universiti Kebangsaan Malaysia, Bangi 43600, Malaysia (e-mail: mardina@ukm.edu.my; nmd@ukm.edu.my).

L. H. Minh is with the Institute of Geophysics, Vietnam Academy of Science and Technology, Hanoi 122118, Vietnam (e-mail: lhminhigp@gmail.com).

N. Floury is with the European Space Agency, 2201 AZ Noordwijk, The Netherlands (e-mail: nicolas.fleury@esa.int).

Color versions of one or more of the figures in this paper are available online at http://ieeexplore.ieee.org.

Digital Object Identifier 10.1109/TGRS.2018.2838321

I. Introduction

THE Biomass mission is envisaged to be launched around 2021 and it is planned to cover a five-year duration. The space segment consists of a single satellite in a near-polar, Sun-synchronous orbit at an altitude of 637–666 km. The orbit is designed to enable repeat pass interferometric acquisitions throughout the mission's lifetime and to minimize the impact of disturbances from the ionosphere [1]. Nevertheless, given the radar working frequency (435 MHz) and the disturbed nature of the low-latitude ionosphere, some special care is being given to the potential corruption that the ionosphere can induce on synthetic aperture radar (SAR) imaging.

The ionosphere can introduce several effects into the Biomass SAR imaging process, such as the following:

1) crosstalk caused by the Faraday rotation;
2) loss of spatial resolution caused by scintillation;

3) azimuthal image shifts caused by total electron content (TEC) spatial gradients.

These effects are determined by the TEC along the propagation path of every pulse emitted by the SAR. The slant TEC derived from Global Navigation Satellite System (GNSS) signals received by ground receivers is a physical quantity, which provides the number of free electrons over 1-m^2 cross-section along the ray path connecting a receiver and a satellite. As the bulk of free electrons is in the ionosphere, a good knowledge of the local features of the equatorial and low-latitude ionosphere can help in optimizing Biomass performance and in decision making such as for the choice of external calibration sites [2]. This is one of the reasons that triggered ESA to support, at the end of 2015, the studies of the upper atmosphere through the Alcantara initiative of the General Studies Program (https://gsp.esa.int/alcantara). Two projects, named Ionospheric Research for Biomass in South America (IRIS) and Ionospheric environment characterization for Biomass Calibration over South East Asia (IBisCo), were among the successful proposals. IRIS and IBisCo released an in-depth climatological description of the Brazilian as well as the Southeast Asian (SEA) equatorial ionospheric anomaly (EIA) used to support Biomass-related investigations. The main objective of this paper is to report the principal findings of the two projects, highlighting the original approach adopted to assess the regional characteristics of TEC, TEC gradients, and scintillations around 6 A.M. and 6 P.M. local times (LTs) of the Biomass orbital passes.

The low-latitude ionosphere is characterized by electron density gradients, termed as blobs and bubbles, which are the signatures of the inhomogeneous distribution of the free electrons resulting from the complex electrodynamics featuring in the region [3]. The daytime equatorial ionosphere presents northward and eastward electric fields generated in the E-region that are mapped along the magnetic field lines to F-region. These electric fields depend strongly on magnetic flux-tube-integrated conductivity. The joint action of magnetic field (**B**) and zonal electric field (**E**) causes an $\mathbf{E} \times \mathbf{B}$ drift that moves plasma upward during day. The uplifted plasma then, under the action of the gravitational force, diffuses to higher latitudes, and two electron density-enhanced regions, defined as "equatorial ionization anomaly crests," appear in both the northern and southern $\pm 15°/\pm 20°$ low-latitude magnetic sectors, leaving a trough at the magnetic equator. This phenomenon is known as the "fountain effect" and gives rise to the EIA [3]–[5]. It is worth highlighting that besides the $\mathbf{E} \times \mathbf{B}$ drift and field-aligned diffusion of plasma, meridional winds modulate the morphology of the EIA, whose crests are raised in the windward hemisphere by trans-equatorial meridional winds through the ion drag effect [6]. After the local sunset, the low-latitude ionosphere presents also an additional peculiar feature: the prereversal enhancement (PRE) [7]. The PRE is superimposed to the daytime upward and nighttime downward drift of plasma, creating the condition for a destabilization of the ionosphere due to the Rayleigh–Taylor instability [8]. Such condition favors the formation of irregularities of several scale sizes resulting in TEC gradients, scintillations, and equatorial spread F (presence of electron density irregularities visible as diffuse echoes on the ionograms at F altitude) [9]. Scintillations appear as phase and amplitude fluctuations of the trans-ionospheric signals received at ground. Ionospheric changes can be even more dramatic during magnetic storms [10].

The choice to design the Biomass mission with the orbital passes at 6 A.M. and 6 P.M. could save the SAR imaging from the ionospheric perturbation occurring mainly in the evening hours. Nevertheless, some degradation could also be observed in the 6 P.M. pass because of the ionospheric instability about to happen in the succeeding hours.

The coupling between ionized and neutral atmosphere can also result in the formation of traveling ionospheric disturbances (TIDs). TIDs are the ionospheric manifestation of gravity waves propagating in the neutral atmosphere [11]. These disturbances are one of the most common ionospheric phenomena that can contribute to TEC perturbations. TIDs are classified into two main categories, namely large-scale TIDs (LSTIDs) with a period greater than 1 h and moving faster than 0.3 km/s, and medium-scale TIDs (MSTIDs) with shorter periods (from 10 min to 1 h) and moving more slowly (0.05–0.3 km/s) (see [12] and the references therein). The origin of MSTIDs is usually attributed to the neutral atmospheric turbulence associated with meteorological activity or to the vertical irradiance gradient associated with the solar terminator (see [12] and the references therein).

The occurrence of external perturbations originating from the Sun and affecting the magnetosphere-ionosphere coupling makes the EIA configuration very different from the one assumed during quiet times. In particular, the EIA crests can disappear, causing the suppression of the ionospheric irregularities producing scintillations. In other cases, the disturbances can intensify the EIA resulting in the exacerbation of scintillations and LSTIDs occurrence [13], [14]. During the same storm, inhibition and intensification of the ionospheric scintillations can concur [15].

This paper focuses on the description of the ionospheric climatology derived from TEC and GNSS scintillation data acquired in the years 2014 and 2015 in Brazil and SEA under quiet geomagnetic conditions. Section II focuses on the data used for the analysis, whereas Section III describes the original approach adopted to highlight the behavior shown by the low-latitude ionosphere at the different observed longitudinal sectors. Section IV describes and discusses the achieved results. Since results for SEA and Brazil present peculiar characteristics, they are described separately. Differences and similarities found in the ionospheric environment of the two regions are reported in the concluding remarks.

II. Data

The ionospheric irregularities appearing as steep TEC gradients describe the inhomogeneous distribution of free electrons in the upper atmosphere. Since TEC is an intrinsic characteristic of the ionosphere, it is independent of the working frequency used to probe the plasma. Differently, as scintillation is an effect induced on the amplitude and phase of the signal, its measurement is frequency-dependent. This means that the use of GNSS data can provide a complete TEC scenario but can only give a partial description of scintillation climatology

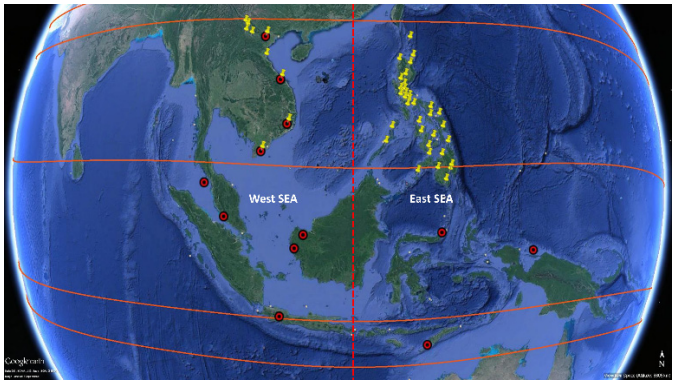

Fig. 1. Location of the GNSS stations (geodetic receivers: pins; scintillation receivers: circles). Orange lines represent the expected position of the geomagnetic equator and the isoclinic lines at magnetic latitude of ±15° and ±20°. Red dashed line indicates the meridian at 115°E.

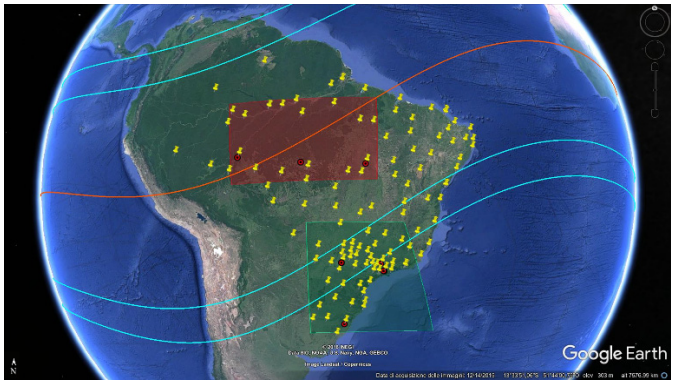

Fig. 2. Location of the GNSS receivers of the RBMC network (yellow pins) used for the TEC analysis and of the GNSS receivers of the LISN and CIGALA (red circles) used for scintillation analysis. The red and green boxes indicate the geographic sector considered for the characterization of the geomagnetic equator (red) and crest (green) regions, respectively. The orange line represents the expected position of the geomagnetic equator, whereas cyan lines indicate the isoclinic lines at magnetic latitude of ±15° and ±20°.

at the P-band (Biomass working frequency). At low latitudes, the worst scintillation effects occur on the amplitude of the signals. The amplitude fluctuations are mainly caused by ionospheric irregularities with the sizes of the order of the first Fresnel zone, which at the (GNSS signals) L-band corresponds to scales of hundreds of meters, while at the P-band corresponds to scales of kilometres. This implies that the L-band scintillation climatology addresses the ionospheric irregularities of one order of magnitude smaller than those causing P-band scintillation [16], [17]. Unfortunately, a long-term coverage of P-band measurements of the ionosphere is not available, so the climatology of scintillation to support Biomass presented here is derived from GNSS data. Nevertheless, an in-depth study of TEC gradients can give important insights on the ionospheric morphology and, in particular, on the different scale sizes of the electron density structures present in the upper atmosphere. Further information can be inferred by the comparison between TEC and the L-band scintillation climatology.

A. Data Providers and Instrumentation

In SEA, the institutions providing the data are: the Institute of Geophysics of the Vietnamese Academy of Science and Technology (Vietnam), Universiti Kebangsaan Malaysia (Malaysia), the National Institute of Aeronautics and Space of Indonesia (Indonesia), and the National Mapping and Resource Information Authority (The Philippines). Such institutions provided Receiver Independent Exchange Format and scintillation data from the stations shown in Fig. 1. The SEA region is divided into two subregions, west and east SEA, with respect to the 115°E meridian.

In South America, in terms of GNSS receivers, the largest network is the Brazilian network for continuous GNSS monitoring (RBMC), managed by the Department of Geodesy of the Brazilian Institute of Geography and Statistics (IBGE). The stations of the Rede Brasileira de Monitoramento Contínuo dos Sistemas GNSS (RBMC)/IBGE network Geocentric Reference System for the Americas. Data from more than 100 GNSS receivers are available under request from the IBGE website (http://www.ibge.gov.br). The Brazilian Space Weather Program (EMBRACE), managed by the National Institute for Space Research (INPE), uses data from RBMC/IBGE to provide TEC products for the technical and scientific communities. A second network of GNSS receivers managed by INPE under the EMBRACE Program is available only for scintillation monitoring. Some of these receivers are also part of the permanent array of instruments from the low-latitude ionospheric sensor network (LISN). The EMBRACE/INPE network consists of 17 GNSS receivers; however, only 6 scintillation monitors have recently been in operation (http://www2.inpe.br/climaespacial/portal/sci-home/). A third network is part of a joint collaboration between the São Paulo State University (Universidade Estadual Paulista), INPE, and the Universidade do Vale do Paraiba. This network was established as a result of the Concept for Ionospheric-Scintillation Mitigation for Professional GNSS in Latin America (CIGALA) and Countering GNSS high Accuracy applications Limitations due to Ionospheric disturbances in Brazil (CALIBRA) projects (European Union/European GNSS Agency Framework Program 7). Although the CIGALA/CALIBRA network can also provide dual-frequency data for TEC investigations, this network was deployed mainly for continuous monitoring of ionospheric scintillations over Brazil. Presently, 10 GNSS receivers for scintillation monitoring are in operation in the CIGALA/CALIBRA network (http://is-cigala-calibra.fct.unesp.br/is/). The sites providing data in Brazil are described in Fig. 2. In Fig. 2, the red and green boxes indicate the geographic sectors considered for the characterization of the geomagnetic equator (red) and crest (green) regions, respectively.

III. Method

To assess the climatology of the ionosphere, we based our analysis on two quietest days provided for each month by the World Data Center for Geomagnetism, Kyoto (http://wdc.kugi.kyoto-u.ac.jp/qddays/index.html) between March 2015 and February 2016 for SEA region and along the entire 2015 for Brazil. These periods have been selected to ensure a good data

coverage and at the same time taking advantage of the data acquired during the EquatoRial Ionosphere Characterization in Asia (ERICA) campaign conducted in SEA [15], [18].

The two quietest days of each month allow the definition of an "average" undisturbed ionosphere, useful to describe the main features of interest for Biomass, which is foreseen to be launched under solar minimum conditions (2021) and to remain in orbit during the ascending period of the next solar cycle. A special focus is given to the times of the foreseen Biomass orbital passes, i.e., local 6 A.M. and 6 P.M. In particular, the monthly variation of TEC and TEC gradients has been derived considering a 1-h window centered around 6 A.M. and 6 P.M.

The ionospheric assessment has been investigated through the study of TEC (including its spatial and temporal variation) and amplitude scintillation (S_4).

A. TEC and TEC Gradients Determination

TEC values are retrieved by using GPS phase and code measurements on L1 and L2. In order to cancel out satellite and receiver interfrequency biases, the calibration technique described in [19] and further detailed in [20] was applied. To obtain the maps of TEC over the regions of interest, the "natural neighbor" interpolation technique has been applied. According to [21], in the case of local maps of TEC, this technique gives better results than other commonly used methods, such as linear, inverse distance weighting, Kriging, and so on. The natural neighbor interpolation technique is based on the identification of the Voronoi cell associated with a set of scattered points in the selected area [22]. The Voronoi polygons network can be constructed through Delauney triangulation of the data [23].

The TEC spatial gradients have been derived from the TEC maps produced with the previously described method. In particular, we have calculated the TEC gradients along both the north–south direction $\Delta\mathrm{TEC}_{N-S}$ and the east–west direction $\Delta\mathrm{TEC}_{E-W}$ with the following equation [20]:

$$\Delta\mathrm{TEC}_{N-S}(\mathrm{GP}_{i,j}) = \frac{\mathrm{TEC}(\mathrm{GP}_{i+1,j}) - \mathrm{TEC}(\mathrm{GP}_{i,j})}{d_i} \quad (1)$$

$$\Delta\mathrm{TEC}_{E-W}(\mathrm{GP}_{i,j}) = \frac{\mathrm{TEC}(\mathrm{GP}_{i,j+1}) - \mathrm{TEC}(\mathrm{GP}_{i,j})}{d_j} \quad (2)$$

where $\Delta\mathrm{TEC}_{N-S}(\mathrm{GP}_{i,j})$ is the TEC gradient along the north–south direction calculated for the point of the grid with coordinates (i, j), $\mathrm{TEC}(\mathrm{GP}_{i+1,j})$ is the TEC value of the first northerly point of the grid with respect to (i, j), $\mathrm{TEC}(\mathrm{GP}_{i,\ j})$ is the TEC value of the considered grid point (i, j), and d_i is the distance between point $(i+1, j)$ and point (i, j). Similar terms are used in (2) in which $\mathrm{TEC}(\mathrm{GP}_{i,\ j+1})$ is the easterly point of the grid with respect to (i, j). Given the density of the considered networks and the division in subregions reported in Section II, the binning of the grid points has been set to 1° latitude ×1° longitude for the east SEA, west SEA, and Brazilian equatorial regions, while 0.5° latitude × 0.5° longitude for the Brazilian crest region.

B. TIDs Detection

Algorithms to detect the presence of TIDs have been run on TEC maps obtained at every 5-min interval, over the regions of interest for the two quietest days, accordingly to what is described previously. The networks used to produce TEC maps are those described in Figs. 1 and 2. TEC data were detrended by subtracting a 4-h running average in each latitude–longitude bin, which is the same as that of the TEC maps. The running average window of 4 h was chosen in order to detect the variations due to both LSTIDs and MSTIDs. The detrended TEC thus contained only its perturbation components and was used to generate the temporal latitudinal and longitudinal TEC perturbation profiles at the corresponding longitudinal and latitudinal sectors, respectively. As our work focused only on the TEC variations associated with TIDs, increases/decreases in the amplitude of the TEC perturbations above/below a threshold of 0.2 total electron content units (TECUs) were used to detect the presence of TIDs. The propagation parameters (period, horizontal drift velocity, and horizontal wavelength) of the detected TIDs were estimated based on the assumption that TIDs propagate as a plane wave. The time lag was determined by running the cross-correlation function on the TEC perturbation profiles and the distance estimated from the latitude and longitude values of the observed TEC perturbations. The apparent velocity was then calculated dividing the distance by the time lag. To determine the period of the TEC perturbations, a fast Fourier transform was then performed on the TEC perturbation temporal profiles. The values for the horizontal wavelength were determined from the values of velocity and time period. In this work, MSTIDs are defined as TEC perturbations that satisfy the following criteria:

1) The TEC perturbation has an amplitude exceeding 0.2 TECU.
2) The horizontal wavelength of the TEC perturbation is smaller than 600 km.
3) The period of the TEC perturbation is lower than 60 min.

The LSTIDs are defined as TEC perturbations that satisfy the following criteria.

1) The TEC perturbation has an amplitude exceeding 0.2 TECU.
2) The horizontal wavelength of the TEC perturbation is larger than 1000 km.
3) The period of the TEC perturbation is greater than 60 min.

After validating the algorithm on midlatitude data by comparing the results with those reported in [24] (not shown here for the sake of conciseness), it was applied on TEC maps generated over SEA and Brazil.

C. Scintillations Occurrence

For what concerns ionospheric scintillation, we concentrated our analysis on the amplitude scintillation index (S4) calculated by a given receiver every minute for each satellite in view. The considered scintillation receivers provide S4 calculated on GPS L1 every minute. To minimize the effect of multipath mimicking actual ionospheric scintillation,

an elevation angle (α_{elev}) mask of 30° was applied. The S4 index is projected to the vertical, with the aim to minimize the effect of the geometry of the GPS receiver network. Such verticalization is performed by deriving S_4^{vert} according to the following formula:

$$S_4^{\text{vert}} = S_4^{\text{slant}} / (F(\alpha_{\text{elev}}))^{\frac{(p+1)}{4}} \tag{3}$$

where S_4^{slant} is the amplitude scintillation index directly measured by the receivers, p is the phase spectral slope, and $F(\alpha_{\text{elev}})$ is the obliquity factor introduced in [25], which is defined as

$$F(\alpha_{\text{elev}}) = \frac{1}{\sqrt{1 - \left(\frac{R_E \cos \alpha_{\text{elev}}}{R_E + H_{\text{IPP}}}\right)^2}}. \tag{4}$$

In (4), R_E is the Earth's radius and H_{IPP} is set to 350 km, where IPP stands for ionospheric piercing point.

The assumptions behind the verticalization are the following:

1) weak scattering regime, which allows the use of [26, Formula (31)] to derive (3);
2) single phase screen approximation, which allows writing the exponent of the obliquity factor in Formula (3) as $(p + 1)/4$.

As the scintillation receivers in the IRIS/IBisCo network do not directly measure the value of the phase spectrum p, some extra assumptions are needed. By following the recommendations of [16], we adopted the same value of $p = 2.6$ introduced in [27], which makes the exponent in (3), which is equal to 0.9. A detailed discussion about the validity and perils of such assumptions is given in [28]. Hereafter, we refer to S_4^{vert} as S_4.

D. TEC Mapping Method Sensitivity

The sensitivity of TEC and TEC gradients mapping to the density of the GNSS network is discussed to assess the reliability of the adopted method. The TEC maps obtained with the GNSS stations from the IBGE-RBMC network covering the southern crest region have been used as the ionospheric truth. Different numbers of fictitious stations located on a regular grid have been used to create the synthetic networks. In particular, five synthetic networks have been considered, with 4, 16, 36, 64, and 100 stations. For each synthetic network, the position of IPPs has been calculated considering the actual position of the GPS satellites, and the corresponding TEC value is sampled from the truth map obtaining the synthetic values of TEC. Such values are finally used to obtain a synthetic map of TEC (through their interpolation) and TEC gradients (according to the method described in Section II-B). Synthetic maps have the same resolution and boundaries of the truth ones. An example of the synthetic receivers' location of the position of the corresponding synthetic IPPs' (calculated on March 10, 2015 at 6 A.M. LT) with respect to the grid points of the ionospheric truth map is provided in Fig. 3.

To provide a figure of merit, differences between truth and synthetic maps of TEC, ΔTEC_{N-S} and ΔTEC_{E-W} have been evaluated for the following days:

1) March 10, 2015 at 6 A.M./P.M.
2) December 30, 2015 at 6 A.M./P.M.

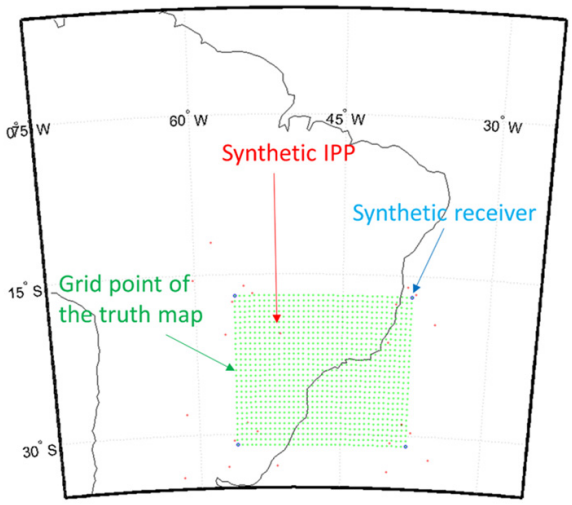

Fig. 3. Example of synthetic receivers' location (four blue dots). Position of the synthetic IPP's (red dots) and the grid point of the ionospheric truth map (green points).

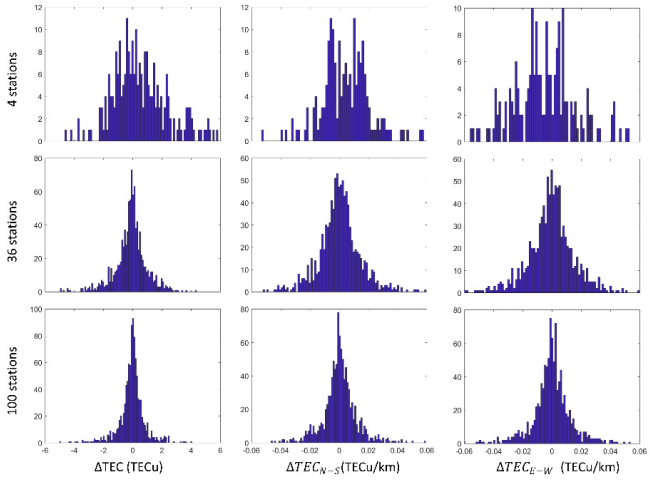

Fig. 4. (Left column) ΔTEC, (Middle column) ΔTEC_{N-S}, and (Right column) ΔTEC_{E-W} considering three different synthetic networks including (Top row) 4, (Middle row) 36, and (Bottom row) 100 stations.

Such days have been selected as they are representative of the equinoctial and solsticial conditions. Results of the sensitivity analysis on December 30, 2015 at 6 P.M. are provided in Fig. 4 as an example. The first, second, and third rows of Fig. 4 report the histograms of the point by point differences between the truth and synthetic maps considering three different synthetic networks made up of 4, 36, and 100 fictitious stations, respectively. First column in Fig. 4 shows the differences (ΔTEC) between TEC_{true} and TEC_{synt}, whereas the second and third columns report the differences ΔTEC_{N-S} and ΔTEC_{E-W}, respectively.

To provide an overview of such results, Fig. 5 reports the standard deviation (SD) of the ΔTEC (top), ΔTEC_{N-S} (middle), and ΔTEC_{E-W} as a function of the number of the synthetic stations. Different colors correspond to the four considered periods, according to the legend. At equinox, the SD is generally larger than at solstice, being up to about

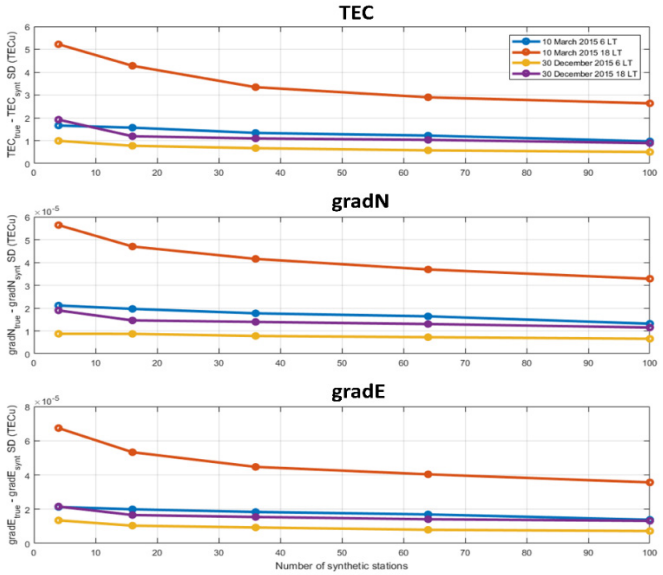

Fig. 5. SD of (Top) TEC, (Middle) ΔTEC_{N-S} gradient, and (Bottom) ΔTEC_{E-W} gradient differences as a function of the number of the synthetic stations. Different colors correspond to the four considered periods.

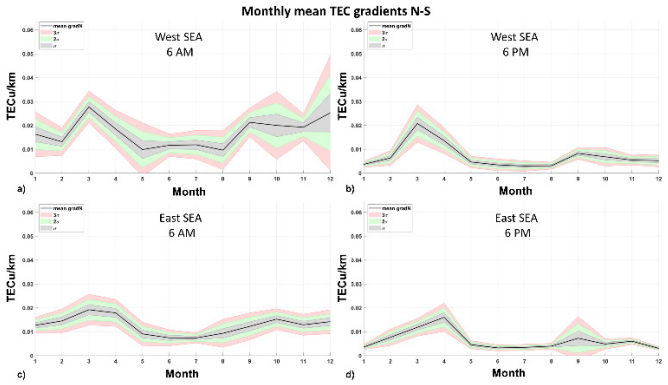

Fig. 6. Monthly variation of the hourly mean TEC gradients (north–south direction) over (a) and (b) west and (c) and (d) east SEA. (a) and (c) refer to 6 A.M. (b) and (d) refer to 6 P.M.

five times larger at 18 LT. Fig. 5 clearly illustrates that the SD saturates when the number of stations increases, indicating that a few tenths of receivers can be sufficient to efficiently cover regions like the one under consideration. Such information is crucial to support the Biomass mission, because it provides a quantitative assessment of the GNSS receivers necessary to provide a realistic picture of the local ionosphere. The sensitivity exercise has been applied on the Brazilian southern crest, because this sector includes many more stations than the SEA region.

IV. Results and Discussion

The results of the analysis conducted according to the method described in Section III are here given in the form of slice plots and graphs to describe the monthly variation of the ionospheric climate in the regions under investigation.

A. SEA Region—TEC Spatial Gradients

Fig. 6 shows the monthly variation of the mean of the absolute value of the TEC gradients at 6 A.M. and 6 P.M.

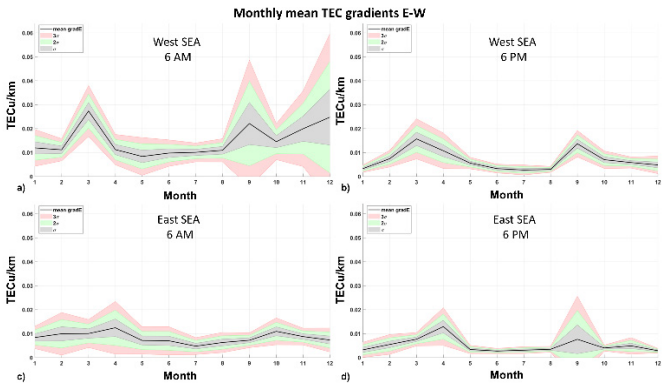

Fig. 7. Monthly variation of the hourly mean TEC gradients (east–west direction) over (a) and (b) west and (c) and (d) east SEA. (a) and (c) refer to 6 A.M. (b) and (d) refer to 6 P.M.

along the N-S direction over west [see Fig. 6(a) and (b)] and east [see Fig. 6(c) and (d)] SEA. In Fig. 6, also the 1 σ (gray), 2 σ (green), and 3 σ (red) variations are reported. To obtain such values, a window of 1 h centered around 6 A.M. and 6 P.M. LT is considered. Over both the sectors, the equinoxes result highly variable at both considered times, even if in the west SEA, the larger variance is found in December at 6 A.M., implying the simultaneous presence of irregularities of different scale sizes during the equinoctial months and around the December solstice. To complete the picture provided, Fig. 7 shows the monthly variation of the mean of the absolute value of the TEC gradients at 6 A.M. and 6 P.M. along the E–W direction over west [see Fig. 7(a) and (b)] and east [see Fig. 7(c) and (d)] SEA. Similar to the N-S gradients, in both SEA regions, the larger gradients and variability are found in the equinoctial months. Also in this case, the variability peak is found in December over west SEA at 6 A.M.

Figs. 8 and 9 show the slice plots of the monthly variation of the TEC mean gradients and their SDs along the north–south and the east–west direction at 6 A.M. and 6 P.M. under west and east SEA. The pictures highlight the seasonal variation, clearly identifying the equinoctial months as the most disturbed. It is interesting to notice the change of sign around 20°N, over both west and east SEA. It is identified by a plateau (mean TEC gradients around 0 TECU/km) that separates the region characterized by positive gradients from the region characterized by negative gradients. As the dip equator is located at 7.5°N, the gradients mapping confirms the presence of the EIA crest around 20°N and the TEC positive and negative slopes before and after the plateau. The west SEA presents a larger variability of the gradients in the proximity of the dip equator. From the SDs, the variability of the meridional gradients results to be larger around the dip equator and the EIA northern crest over the west SEA. The zonal gradients over west SEA result positive and negative according to the longitudinal sectors. Over west SEA, the equinoctial and December months are clearly identified as the best candidates to host the greater zonal gradients. In the same sector, the signatures of the crest and the dip equator is recognizable. Over east SEA, the zonal gradients are very low and evenly distributed, and the crest signature is visible just between 15°N–20°N and at the highest longitude.

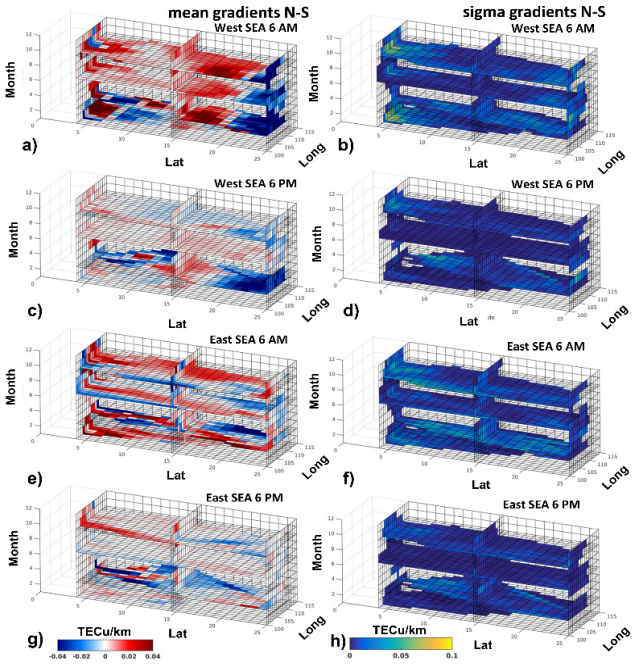

Fig. 8. Slice plots of the monthly variation of (a), (c), (e), and (g) TEC mean gradients along the north–south direction and (b), (d), (f), and (h) their SDs over (a)–(d) west and (e)–(h) east SEA at 6 A.M. and 6 P.M.

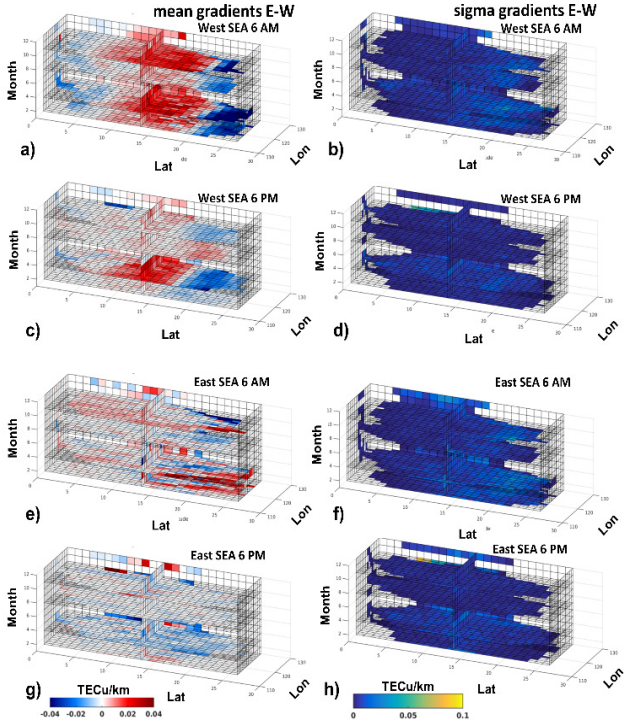

Fig. 9. Slice plots of the monthly variation of (a), (c), (e), and (g) TEC mean gradients along the east–west direction and (b), (d), (f), and (h) their SDs over (a)–(d) west and (e)–(h) east at 6 A.M. and 6 P.M.

The variability shown by the SD is quite low over both west and east SEA, with a slight enhancement over the dip equator and within the crest.

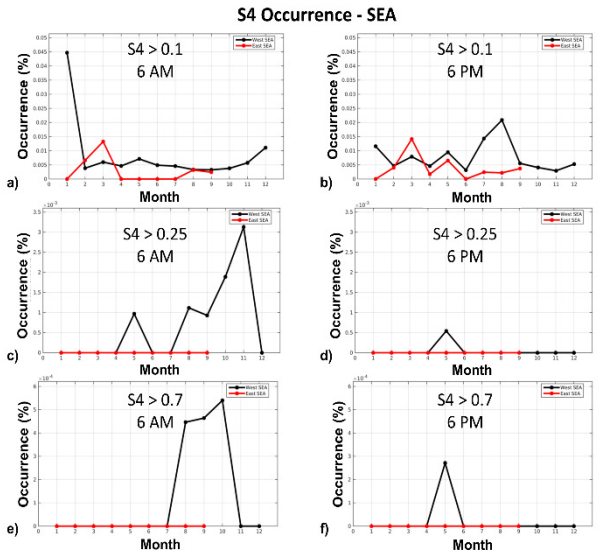

Fig. 10. Monthly variation of the S4 occurrence above three levels of scintillation over east (red curves) and west (black curves) SEA. (a), (c), and (e) refer to 6 A.M. (b), (d), and (f) refer to 6 P.M.

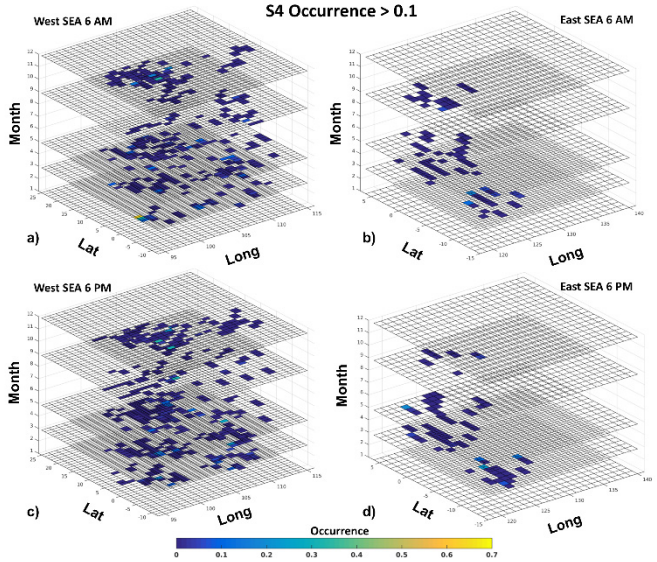

Fig. 11. Slice plots of the monthly variation of the S4 occurrence above 0.1 over (a) and (c) west and (b) and (d) east SEA.

B. SEA Region—Scintillations

The monthly variation of the scintillation occurrence were produced over the east and west SEA, covering the region between the dip equator and the southern EIA crest, as well as the region of the dip equator and the two EIA crests, respectively (see Fig. 10). The occurrence was sorted according to three levels of amplitude scintillations: $S_4 > 0.1$, $S_4 > 0.25$, and $S_4 > 0.7$, and by considering a 1-h window centered at 6 A.M. and 6 P.M. LT.

The seasonal behavior shows how the equinoctial maxima characterize all the levels of scintillations (from weak to strong scattering regimes). A gap in the data from October to December 2015 and in January 2016 does not allow to characterize the seasonal variation in the east SEA region.

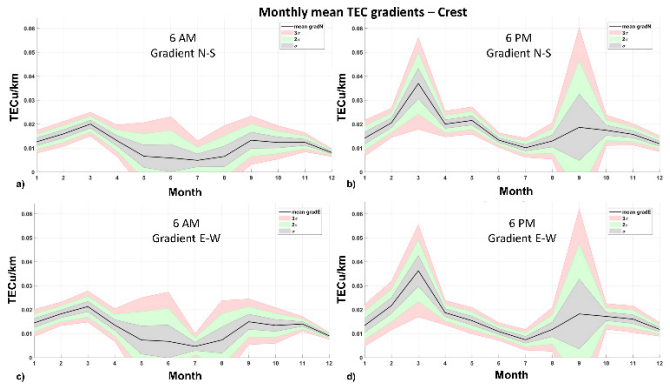

Fig. 12. Monthly variation of the hourly mean TEC gradients along (a) and (b) north–south and (c) and (d) east–west directions under the EIA southern crest at (a) and (c) 6 A.M. and (b) and (d) 6 P.M.

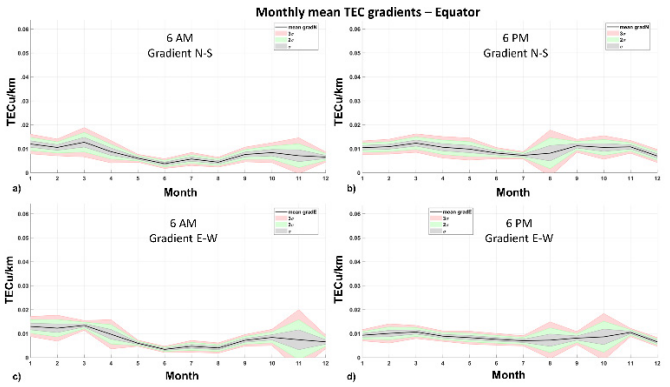

Fig. 13. Monthly variation of the hourly mean TEC gradients along (a) and (b) north–south and (c) and (d) east–west directions under the dip equator at (a) and (c) 6 A.M. and (b) and (d) 6 P.M.

TABLE I

APPARENT VELOCITY, TIME PERIOD, AND WAVELENGTH OF THE MSTID DETECTED IN THE SEA REGION ON AUGUST 30, 2015

Day number	Apparent velocity (km/s)	Time period (minutes)	Wavelength (km)
242/2015	0.0722	45	195

The monthly variation of the scintillation occurrence for $S_4 > 0.1$ west and east SEA is shown in the slice plots of Fig. 11. Even though the seasonal scenario over east SEA is not completed because of the data gap from October to December 2015 and in January 2016, Fig. 11 shows the presence of scintillations in the spring equinox at both 6 A.M. and 6 P.M. in the east SEA region. The seasonal behavior in the west SEA shows a fairly even distribution of scintillation all year long during both time intervals

C. SEA Region—TIDs

The TIDs detection algorithms were applied on TEC maps used for TEC gradients analysis as described in Section II-B.

It was observed that none of the analyzed days revealed the presence of LSTIDs over this region. It is well known that the LSTIDs are generally observed during geomagnetic storms, as these are mainly generated by Joule heating produced from intense particle precipitation in the auroral and subauroral regions [13], [14]. All the days analyzed in this paper are geomagnetically quiet and therefore not associated with any disturbances, which agrees with the absence of LSTIDs.

A MSTID was detected only on one day. The estimated parameters are shown in Table I.

D. Brazil—TEC Spatial Gradients

Fig. 12(a) and (b) shows the monthly variation of the mean of the absolute value of the TEC gradients along the N-S direction under the EIA southern crest. The maxima are located in March and between September and October, confirming a higher degree of ionospheric disturbance during the equinoctial months. Moreover, the gradients are generally larger around 6 P.M. than around 6 A.M. It is interesting to notice the intense scattering of the gradients observed in May and June at 6 A.M. Such feature implies the simultaneous presence of irregularities of different scale sizes during such months.

Fig. 12(c) and (d) shows the monthly variation of the mean of the absolute value of the TEC gradients along E-W direction under the EIA southern crest. At 6 P.M. [see Fig. 12(d)], the maxima are found during the equinoxes (in March and September) and the minima occur in July and between December and January. This is exactly the same pattern found for the meridional gradients in the same time interval. At 6 A.M. [see Fig. 12(c)], again three maxima are present: March, June, and September. Also, in this case, the strongest scattering of the gradients is found during equinoxes and winter, indicating the presence of different scale sizes of the ionospheric structuring also along the east–west direction.

Fig. 13(a) and (b) shows the monthly variation of the mean of the absolute value of the TEC gradients along the N-S direction over the dip equator. In Fig. 13, plots have been obtained considering a 1-h window centered at 6 A.M. [see Fig. 13(a)] and 6 P.M. [see Fig. 13(b)].

Comparing the panels of Fig. 13 with the corresponding ones in Fig. 12, the lower values of the gradients over the dip equator with respect to those recorded under the southern crest of the EIA are evident. The main differences arise at 6 P.M. At 6 A.M., again three maxima are present: March, July, and November. At 6 P.M., the largest variability of the ionospheric structuring close to the equator is found in August, and two maxima are found in March and in October, even if less pronounced than in the case of 6 A.M. Fig. 13(c) and (d) reports the same as Fig. 13(a) and (b) but for the zonal gradient. In this case, again the values are generally lower than those under the crest. At 6 A.M., largest variability gradients are found in November and between January and April. Minimum values and variability are found in the winter time. At 6 P.M., the largest variability of the gradients is found in August and October.

Figs. 14 and 15 show the 3-D representation of the monthly variation of the TEC mean gradients and their SDs along the north–south direction and east–west direction under the

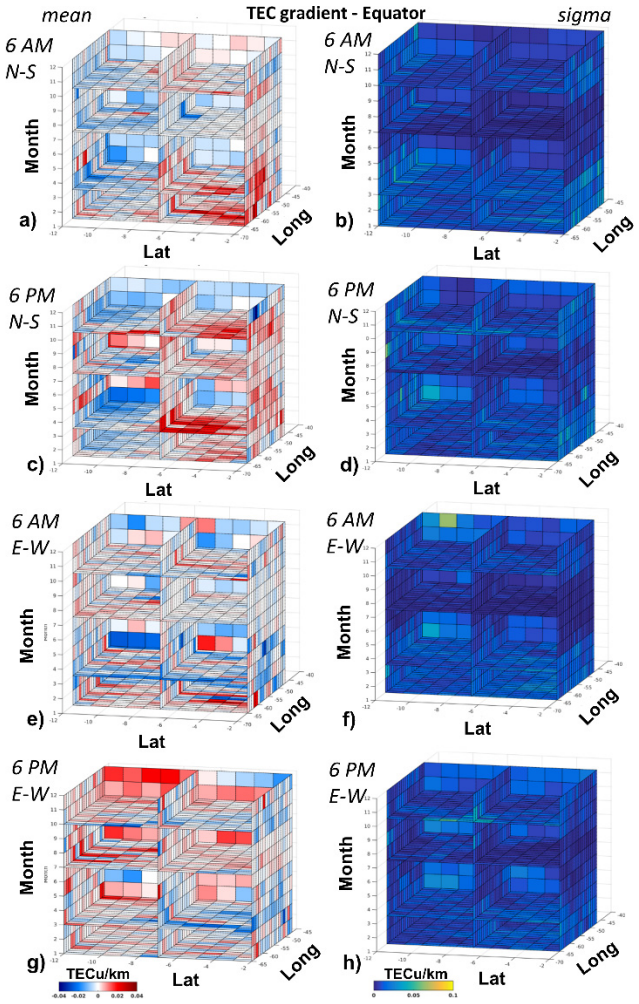

Fig. 14. Slice plots of the monthly variation of (a), (c), (e), and (g) TEC mean gradients along the north–south direction and east–west direction and (b), (d), (f), and (h) their SDs over the dip equator at 6 A.M. and 6 P.M.

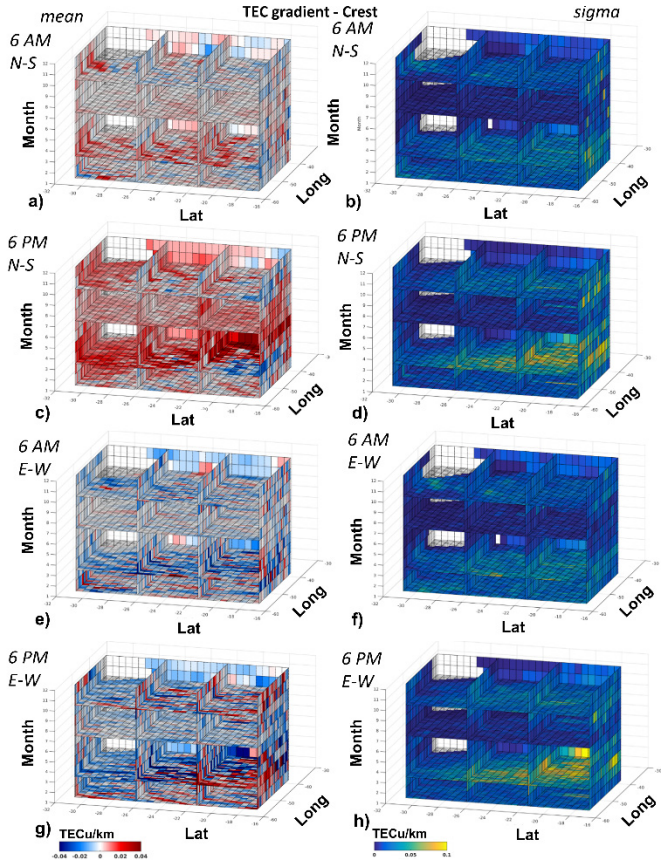

Fig. 15. Slice plots of the monthly variation of (a), (c), (e), and (g) TEC mean gradients along the north–south direction and east–west direction and (b), (d), (f), and (h) their SDs over the EIA southern crest at 6 A.M. and 6 P.M.

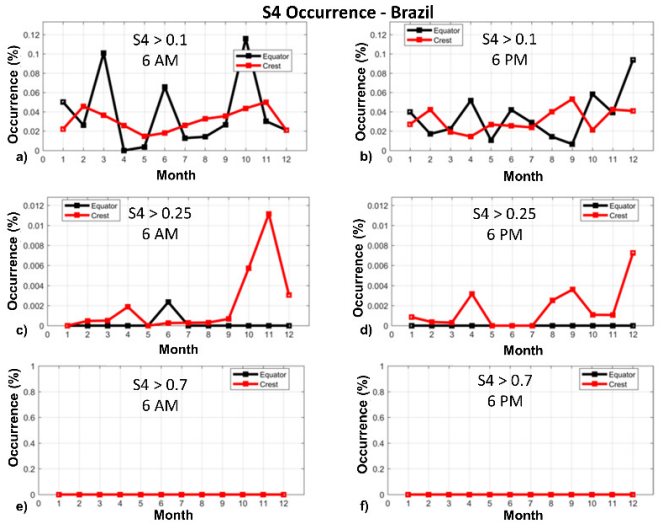

Fig. 16. Monthly variation of the S4 occurrence above three levels of scintillation under the EIA southern crest (red curves) and around the dip equator (black curves). (a), (c), and (e) refer to 6 A.M. (b), (d), and (f) refer to 6 P.M.

dip equator (see Fig. 14) and around the EIA southern crest (see Fig. 15) at 6 A.M. and at 6 P.M.

Figs. 14 and 15 highlight how the meridional TEC gradients increase during the equinoctial months (March and October) and present a high degree of variability of the ionospheric structuring. It is interesting to notice the change of sign (negative gradients) around the same months in the region of the crest closer to the dip equator (located around −9°N), corresponding to the highest degree of variability shown by the SD. The zonal gradients show a larger variability in the sign but confirm the presence of the ionospheric irregularities of different scale sizes mainly in March and also in October. The change of sign (positive gradients) around the same months in the region of the crest closer to the dip equator (located around −9°N) appears similar to the one identified in the N-S gradients.

In the dip equator (see Fig. 14), the monthly variation of the meridional gradients shows significant values but with a meaningfully lower variability with respect to those observed in the crest. The E-W gradients show the same scenario; gradients comparable with those found under the crest (see Fig. 15) but with a significantly lower variability. This means that around the dip equator, the ionospheric structuring along the east–west and along the N-S direction is less variable than in the crest.

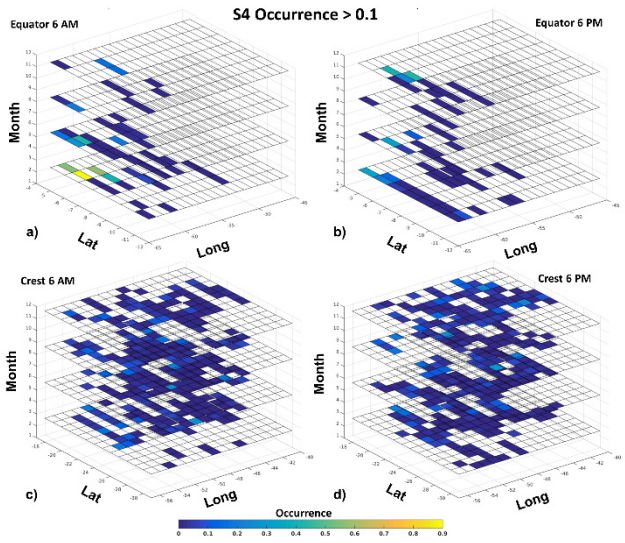

Fig. 17. Slice plots of the monthly variation of the S4 occurrence above 0.1 (Top) in the dip equator and (Bottom) within the EIA southern crest. (a) and (c) refer to 6 A.M. (b) and (d) to refer 6 P.M.

E. Brazil—Scintillations

The monthly variation of the S_4 occurrence for the three levels of amplitude scintillation ($S_4 > 0.1$, $S_4 > 0.25$, and $S_4 > 0.7$), considering the two 1-h windows centered at 6 A.M. and 6 P.M. is given in Fig. 16. The seasonal behavior shown in Fig. 16 highlights that, on a statistical base, there is no occurrence of strong scintillation events at 6 A.M. and 6 P.M. in neither the crest nor the dip equator [see Fig. 16(e) and (f)]. The equinoctial maxima characterize mainly the moderate scattering regimes of the crest region [see Fig. 16(c) and (d)] and the weak scattering regime of the equatorial region [see Fig. 16(a) and (b)]. The equatorial region is also characterized by an increase of the occurrence in June for the weak scattering regime [see Fig. 16(a) and (b)] at both 6 A.M. and 6 P.M., and for the moderate scattering regime at 6 A.M. [see Fig. 16(c)]. The two regions present a similar seasonal behavior of the weak scintillation ($S_4 > 0.1$) occurrence (see Fig. 17).

F. Brazil—TIDs

Algorithms to detect the presence of TIDs were applied on TEC maps obtained at every 5-min interval, over the equatorial and anomaly crest regions in Brazil (see Section II.2 for the method). The TEC maps for the equatorial regions covered a spatial range of −12.0°N to −2.0°N in IPP latitude and −65.0°E to −47.0°E in IPP longitude with a 1° resolution, while over the anomaly crest regions, they covered a spatial range of −31.0°N to −17.0°N in IPP latitude and −56.0°E to −38.0°E in IPP longitude with a 0.5° resolution.

It was observed that none of the analyzed days revealed the presence of LSTIDs over these regions, as expected during geomagnetically quiet conditions.

TABLE II
APPARENT VELOCITY, TIME PERIOD, AND WAVELENGTH OF THE DETECTED MSTIDS

Day number	Apparent velocity (km/s)	Time period (minutes)	Wavelength (km)	Region
018	0.124	14	106	Crest
226	0.0833	25	125	Equator
329	0.1852	45	500	Equator

The MSTIDs were detected on one day over the crest and on two days over the equatorial region during the year 2015. The main characteristics of the MSTIDs observed over the crest and equatorial region are summarized in Table II.

V. CONCLUSION

The TEC gradients characterizing the low-latitude ionosphere can degrade the quality of the imaging that the P-band SAR on board the future Biomass ESA mission will provide. The original approach proposed in this paper offers a climatological picture of the low-latitude ionosphere properly customized to provide the information needed for the Biomass mission operational purposes. Such information cannot be entirely derived from the global models of the ionosphere. This is the reason why this paper is proposed as a valuable contribution to the regional characterization of the ionospheric impact on remote sensing.

Space weather introduces a high level of ionospheric unpredictability in the SEA and Brazilian regions due to the complex dynamics occurring in the proximity of the EIA. Indeed, TEC variations and scintillation occurrence can be very different from case to case, often being associated with very fine structuring of the ionospheric plasma. This means that a reliable assessment of the ionospheric scenario, even during quiet times, must rely on data-driven representation. Indeed, our statistical analysis of the TEC gradients and scintillations reveals the following:

1) An important distinction between the meridional TEC variation and the zonal variation in both regions are under investigation.
2) A clear definition of the role of EIA crests in hosting the ionospheric irregularities.
3) Peculiar characteristics of the low-latitude ionosphere at the Biomass orbital passes (6 A.M. and 6 P.M.).
4) The contribution of MSTIDs to TEC variations is minor but not negligible during quiet time.

Our assessment of the sensitivity of the method adopted to calculate both TEC and corresponding gradients to the number of the receivers in the network indicates that a few tenths of receivers can be sufficient to provide a reliable climatology over regions like the one considered in Brazil.

REFERENCES

[1] *Report for Mission Selection: Biomass, ESA SP-1324/1 (3 Volume Series)*, Eur. Space Agency, Noordwijk, The Netherlands, 2012.

[2] S. Quegan *et al.*, "Ionospheric mitigation schemes and their consequences for Biomass product quality," Eur. Space Agency, Paris, France, Tech. Rep., 2012. [Online]. Available: ftp://ftp.shef.ac.uk/pub/uni/projects/ctcd/NeilRogers/Technical_Data_Package/Reports/BIOMASS_Iono_Study_Final_Report%20(short%20version).pdf

[3] M. C. Kelley, *The Earth's Ionosphere Plasma Physics and Electrodynamics* (International Geophysics Series), vol. 43. San Diego, CA, USA: Academic, 1989.

[4] E. V. Appleton, "Two anomalies in the ionosphere," *Nature*, vol. 157, no. 3995, p. 691, 1946.

[5] R. A. Heelis, "Electrodynamics in the low and middle latitude ionosphere: A tutorial," *J. Atmos. Sol.-Terr. Phys.*, vol. 66, no. 10, pp. 825–838, 2004.

[6] N. Balan and G. J. Bailey, "Equatorial plasma fountain and its effects: Possibility of an additional layer," *J. Geophys. Res.*, vol. 100, no. A11, pp. 21421–21432, 1995, doi: 10.1029/95JA01555.

[7] R. F. Woodman, "Vertical drift velocities and east-west electric fields at the magnetic equator," *J. Geophys. Res.*, vol. 75, no. 31, pp. 6249–6259, 1970, doi: 10.1029/JA075i031p06249.

[8] S. Chatterjee, S. K. Chakraborty, B. Veenadhari, and S. Banola, "A study on ionospheric scintillation near the EIA crest in relation to equatorial electrodynamics," *J. Geophys. Res. Space Phys.*, vol. 119, no. 2, pp. 1250–1261, 2014, doi: 10.1002/2013JA019466.

[9] S. Basu *et al.*, "Scintillations, plasma drifts, and neutral winds in the equatorial ionosphere," *J. Geophys. Res.*, vol. 101, no. A12, pp. 26795–26809, 1996.

[10] M. Mendillo, "Storms in the ionosphere: Patterns and processes for total electron content," *Rev. Geophys.*, vol. 44, p. RG4001, 2006, doi: 10.1029/2005RG000193.

[11] C. O. Hines, "Internal atmospheric gravity waves at ionospheric heights," *Can. J. Phys.*, vol. 38, no. 11, pp. 1441–1481, 1960, doi: 10.1139/p60-150.

[12] M. Hernández-Pajares, J. M. Juan, and J. Sanz, "Medium-scale traveling ionospheric disturbances affecting GPS measurements: Spatial and temporal analysis," *J. Geophys. Res.*, vol. 111, p. A07S11, 2006, doi: 10.1029/2005JA011474.

[13] K. Hocke and K. Schlegel, "A review of atmospheric gravity waves and travelling ionospheric disturbances: 1982-1995," *Ann. Geophys.*, vol. 14, no. 9, pp. 917–940, 1996.

[14] R. D. Hunsucker, "Atmospheric gravity waves generated in the high-latitude ionosphere: A review," *Rev. Geophys.*, vol. 20, no. 2, pp. 293–315, 1982.

[15] L. Spogli *et al.*, "Formation of ionospheric irregularities over Southeast Asia during the 2015 St. Patrick's Day storm," *J. Geophys. Res. Space Phys.*, vol. 121, no. 12, pp. 12211–12233, 2016, doi: 10.1002/2016JA023222.2016.

[16] A. W. Wernik, J. A. Secan, and E. J. Fremouw, "Ionospheric irregularities and scintillation," *Adv. Space Res.*, vol. 31, no. 4, pp. 971–981, 2003.

[17] A. W. Wernik, L. Alfonsi, and M. Materassi, "Ionospheric irregularities, scintillation and its effect on systems," *Acta Geophys. Polonica*, vol. 52, no. 2, pp. 237–249, 2004.

[18] G. Povero *et al.*, "Ionosphere monitoring in South East Asia in the ERICA study," *Navigation*, vol. 64, no. 2, pp. 273–287, 2017, doi: 10.1002/navi.194.

[19] L. Ciraolo, F. Azpilicueta, C. Brunini, A. Meza, and S. M. Radicella, "Calibration errors on experimental slant total electron content (TEC) determined with GPS," *J. Geodesy*, vol. 81, no. 2, pp. 111–120, 2007.

[20] C. Cesaroni *et al.*, "L-band scintillations and calibrated total electron content gradients over Brazil during the last solar maximum," *J. Space Weather Space Climate*, vol. 5, p. A36, Dec. 2015.

[21] M. P. Foster and A. N. Evans, "An evaluation of interpolation techniques for reconstructing ionospheric TEC maps," *IEEE Trans. Geosci. Remote Sens.*, vol. 46, no. 7, pp. 2153–2164, Jul. 2008, doi: 10.1109/TGRS.2008.916642.2008.

[22] A. Okabe, B. Boots, and K. Sugihara, "Nearest neighbourhood operations with generalized Voronoi diagrams: A review," *Int. J. Geogr. Inf. Syst.*, vol. 8, no. 1, pp. 43–71, 1994, doi: 10.1080/02693799408901986.

[23] D. T. Lee and B. J. Schachter, "Two algorithms for constructing a Delaunay triangulation," *Int. J. Comput. Inf. Sci.*, vol. 9, no. 3, pp. 219–242, 1980, doi: 10.1007/BF00977785.1980.

[24] C. Cesaroni *et al.*, "The first use of coordinated ionospheric radio and optical observations over italy: Convergence of high-and low-latitude storm-induced effects," *J. Geophys. Res. Space Phys.*, vol. 122, no. 11, pp. 11794–11806, 2017, doi: 10.1002/2017JA024325.

[25] A. J. Mannucci, B. D. Wilson, and C. D. Edwards, "A new method for monitoring the Earth's ionospheric total electron content using the GPS global network," in *Proc. ION-GPS*, 1993, pp. 1323–1332.

[26] C. L. Rino, "A power law phase screen model for ionospheric scintillation: 1. Weak scatter," *Radio Sci.*, vol. 14, no. 6, pp. 1135–1145, 1997, doi: 10.1029/RS014i006p01135.

[27] L. Spogli, L. Alfonsi, G. De Franceschi, V. Romano, M. H. O. Aquino, and A. Dodson, "Climatology of GPS ionospheric scintillations over high and mid-latitude European regions," *Ann. Geophys.*, vol. 27, no. 9, pp. 3429–3437, 2009.

[28] L. Spogli *et al*, "Assessing the GNSS scintillation climate over Brazil under increasing solar activity," *J. Atmos. Sol.-Terr. Phys.*, vols. 105–106, pp. 199–206, Dec. 2013.

Lucilla Alfonsi received the M.Sc. degree in physics from the Sapienza University of Rome, Rome, Italy, and the Ph.D. degree in geophysics from the Alma Mater Studiorum, Università di Bologna, Bologna, Italy.

She is currently an expert in the investigation of ionospheric irregularities from ground-based and from *in situ* measurements, and ionospheric modeling. She is also the Principal Investigator of the Ionospheric Research for Biomass in South America Project.

Gabriella Povero received the M.Sc. degree in electronics engineering from the Politecnico di Torino, Turin, Italy.

Since 2003, she has been with the Istituto Superiore Mario Boella, Turin, where she is responsible for the unit International Cooperation in GNSS in the Navigation Technologies Research Area. She is also the Principal Investigator of the Ionospheric Environment Characterization for Biomass Calibration over South East Asia Project.

Luca Spogli received the M.Sc. and Ph.D. degrees in physics from Roma Tre University, Rome, Italy.

Since 2008, he has been a Researcher with the Upper Atmosphere Physics Group, Istituto Nazionale di Geofisica e Vulcanologia, Rome. He is currently an expert in ionospheric physics, modeling, data analysis, and treatment techniques.

Claudio Cesaroni received the M.Sc. degree in physics from the Sapienza University of Rome, Rome, Italy, and the Ph.D. degree in geophysics from the University of Bologna, Bologna, Italy.

Since 2015, he has been a Researcher with the Istituto Nazionale di Geofisica e Vulcanologia, Rome, where he is involved in total electron content calibration technique, the effects of spatial and temporal gradients on Global Navigation Satellite System signals, and ionospheric models development and validation.

Biagio Forte received the Ph.D. degree in geophysics from the Karl-Franzens University of Graz, Graz, Austria.

He is currently a Lecturer with the Centre for Space, Atmospheric and Oceanic Science, Department of Electronic and Electrical Engineering, University of Bath, Bath, U.K. He is an expert in the physics and chemistry of the upper ionized atmosphere, plasma turbulence and instabilities, and radio-wave scintillation.

Cathryn N. Mitchell received the Ph.D. degree from the University of Wales, Aberystwyth, U.K.

She is currently a Professor with the Centre for Space, Atmospheric and Oceanic Science, Department of Electronic and Electrical Engineering, University of Bath, Bath, U.K. She is an expert in satellite navigation systems and signal processing.

Robert Burston is currently a Research Fellow with the Centre for Space, Atmospheric and Oceanic Science, Department of Electronic and Electrical Engineering, University of Bath, Bath, U.K.

Sreeja Vadakke Veettil is currently a Senior Research Fellow with the Nottingham Geospatial Institute, University of Nottingham, Nottingham, U.K. Her research interests include assessing the effects of space weather on GNSS receivers and positioning errors aiming to improve the modeling of scintillation and to develop mitigation tools.

Marcio Aquino received the Ph.D. degree in space geodesy from the Institute of Engineering Surveying & Space Geodesy, University of Nottingham, Nottingham, U.K.

He is currently an Associate Professor with the Faculty of Engineering, University of Nottingham, where he leads the Nottingham Geospatial Institute research theme Propagation Effects on Global Navigation Satellites Systems (GNSS). He is also a Geodesist. He has been involved in mitigation of ionospheric effects on GNSS since 2001.

Virginia Klausner received the master's degree in physics and astronomy from the Universidade do Vale do Paraíba (UNIVAP), São José dos Campos, Brazil, in 2007, and the Ph.D. degree in geophysics from the National Observatory, Rio de Janeiro, Brazil, in 2012.

She is currently an Assistant Professor with UNIVAP. Her research interests include signal processing for geosciences, with an emphasis on aeronomy and space geophysics.

Marcio T. A. H. Muella received the B.E. degree in electrical and electronic engineering from the Universidade do Vale do Paraíba (UNIVAP), São José dos Campos, Brazil, in 2002, and the M.Sc. and Ph.D. degrees in space geophysics from the National Institute for Space Research, São José dos Campos, in 2004 and 2008, respectively.

He is currently an Associate Professor with the School of Engineering, UNIVAP, and with the Institute of Research and Development, UNIVAP. He is involved in ionospheric research where the main and in Global Navigation Satellites System-related topics.

Michael Pezzopane received the M.Sc. degree in physics from the Sapienza University of Rome, Rome, Italy, and the Ph.D. degree in geophysics from the University of Bologna, Bologna, Italy.

He has been a Researcher with the Istituto Nazionale di Geofisica e Vulcanologia, Rome, since 2001. His research interests include radio-wave propagation in the ionosphere, electron-density irregularities at low latitudes, ionogram autoscaling, and ionospheric modeling.

Alessandra Giuntini received the M.Sc. degree in physics from Roma Tre University, Rome, Italy, and the Ph.D. degree in geophysics from Bologna's Alma Mater Studiorum University, University of Bologna, Bologna, Italy.

Since 2007, she has been a Researcher with the Istituto Nazionale di Geofisica e Vulcanologia, Rome. Her research interests include seismic location, data analysis, and communication fields.

Ingrid Hunstad received the M.Sc. degree in physics from the Sapienza University of Rome, Rome, Italy, in 1993, and the Specialization degree (Ph.D. equivalent) in geophysics from the Istituto Nazionale di Geofisica e Vulcanologia (INGV), Rome, in 1997.

She is currently a Researcher with the Upper Atmosphere Physics Research Unit, INGV. She is an expert in Global Navigation Satellites System (GNSS) systems expertise, management of the GNSS network for scintillation, and total electron content monitoring.

Giorgiana De Franceschi received the Ph.D. degree *(summa cum laude)* in physics from the Università degli Studi La Sapienza, Rome, Italy, in 1981.

She is currently the Director of Research at the Istituto Nazionale di Geofisica e Vulcanologia, Rome. Her research interests include the temporal/spatial modeling of the high- and low-latitude ionosphere.

Dr. De Franceschi has been elected as a Vice-Chair of the International Union on Radio Sciences Commission G in 2017.

Elvira Musicò received the M.Sc. degree in physics from the Alma Mater Studiorum from the University of Bologna, Bologna, Italy, in 2014, and the Ph.D. degree from the Sapienza University of Rome, Rome, Italy, in 2018.

Since 2012, she has been part of the Upper Atmosphere Physics Group, Istituto Nazionale di Geofisica e Vulcanologia, Rome, where she is involved in the study of global navigation satellite system data and interferometric SAR images.

Marco Pini received the Ph.D. degree in electronics and communications from the Politecnico di Torino University, Turin, Italy.

He is currently the Head of the Navigation Technologies Research Area, Istituto Superiore Mario Boella, Turin. His research interests include baseband signal processing on new Global Navigation Satellites System signals, multifrequency RF front-end design, and software radio receivers.

Vinh La The received the M.Sc. degree in computer engineering from the Hanoi University of Technology, Hanoi, Vietnam, and the Ph.D. degree in computer engineering from Kyung Hee University, Seoul, South Korea.

He is currently the Vice Director of the Navis Centre, Hanoi University of Science and Technology, and also an Assistant Professor with the School of Information and Communication Technology, Hanoi University of Science and Technology.

Hieu Tran Trung received the Engineering degree from the School of Information and Communication Technology, Hanoi University of Science and Technology, Hanoi, Vietnam, and the Ph.D. degree in electronics and communications engineering from the Politecnico di Torino, Turin, Italy.

He is currently with the Navis Centre, Hanoi University of Science and Technology. His research interests include Global Navigation Satellites System (GNSS) software receivers and GNSS integrity.

Asnawi Husin received the M.Sc. degree from the Department of Electrical Electronic Engineering, National University of Malaysia, Bangi, Malaysia, in 2011.

Since 2000, he has been a permanent Researcher with the Ionospheric and Telecommunication Division, Space Science Center, National Institute of Aeronautics and Space, Jakarta, Indonesia. He is involved in ionospheric space weather, and processing and analyzing Global Navigation Satellites System and ionosonde data.

Sri Ekawati received the B.S. degree in physics from Padjadjaran University, Bandung, Indonesia, in 2005, and the M.S. degree in physics from the Bandung Institute of Technology, Bandung, in 2014.

Since 2006, she has been with the Space Science Center, National Institute of Aeronautics and Space, as an Ionospheric and Magnetospheric Researcher.

Charisma Victoria de la Cruz-Cayapan received the B.Sc. and M.Sc. degrees in geodetic engineering and geomatics from the University of the Philippines, Quezon City, Philippiness and a Specializing Master in Navigation and Related Applications (GNSS) from the Politecnico di Torino.

She is Engineer at the National Mapping and Resource Information Authority.

Mardina Abdullah is currently a Professor with the Department of Electrical, Electronic and Systems Engineering, Space Science Centre, Universiti Kebangsaan Malaysia, Bangi, Malaysia.

She is an expert in ionospheric prediction and irregularities, space weather impact on GPS, and GPS satellite error mitigation.

Noridawaty Mat Daud is currently a Research Officer with the Space Science Centre, Universiti Kebangsaan Malaysia, Bangi, Malaysia.

Le Huy Minh received the Ph.D. degree in internal geophysics from the Institut de Physique du Globe de Paris, Paris, France, in 1995.

Since 2003, he has been with the Institute of Geophysics (IGP), Vietnam Academy of Science and Technology, Hanoi, Vietnam, as a Senior Researcher. From 2001 to 2013, he was the Deputy Director of IGP.

Nicolas Floury received the M.Sc. degree in engineering from Télécom ParisTech, Paris, France, and the Ph.D. degree in applied physics from the University Paris Diderot, Paris.

He is currently the Head of the Wave Interaction and Propagation Section at European Space Agency, Noordwijk, The Netherlands.